ARTICLE

Enhancement of Ni– $(Y_2O_3)_{0.08}(ZrO_2)_{0.92}$ fuel electrode performance by infiltration of $Ce_{0.8}Gd_{0.2}O_{2-\delta}$ nanoparticles

Beom-Kyeong Park, Roberto Scipioni, Dalton Cox and Scott A. Barnett*

Received 00th January 20xx, Accepted 00th January 20xx

DOI: 10.1039/x0xx00000x

This paper addresses the use of $Ce_{0.8}Gd_{0.2}O_{2-\delta}$ (GDC) infiltration into the Ni– $(Y_2O_3)_{0.08}(ZrO_2)_{0.92}$ (YSZ) fuel electrode of solid oxide cells (SOCs) for improving their electrochemical performance in fuel cell and electrolysis operation. Although doped ceria infiltration into Ni-YSZ has recently been shown to improve the electrode performance and stability, the mechanisms defining how GDC impacts electrochemical characteristics are not fully delineated. Furthermore, the electrochemical characteristics have not yet been determined over the full range of conditions normally encountered in fuel cell and electrolysis operation. Here we present a study of both symmetric and full cells aimed at understanding the electrochemical mechanisms of GDC-modified Ni-YSZ over a wide range of fuel compositions and temperatures. Single-step GDC infiltration at an appropriate loading substantially reduced the polarization resistance of Ni-YSZ electrodes in electrolyte-supported cells, as measured using electrochemical impedance spectroscopy (EIS) at various temperatures (600-800 °C) in a range of H₂O-H₂ mixtures (3-90 vol.% H₂O). Fuel-electrode-supported cells had significant concentration polarization due to the thick Ni-YSZ supports. A distribution of relaxation times approach is used to develop a physically-based electrochemical model; the results show that GDC reduces the reaction resistance associated with three-phase boundaries, but also appears to improve oxygen transport in the electrode. Increasing the H₂O fraction in the H₂-H₂O fuel mixture reduced both the threephase boundary resistance and the gas diffusion resistance for Ni-YSZ; with GDC infiltration, the electrode resistance showed less variation with fuel composition. GDC infiltration improved the performance of fuel-electrode-supported full cells, which yielded a maximum power density of 2.28 W cm⁻² in fuel cell mode and an electrolysis current density at 1.3 V of 2.22 A cm $^{-2}$, both at 800 °C.

1. Introduction

The solid oxide cell (SOC) is an electrochemical device that efficiently converts between chemical energy (fuels such as H_2 and CH_4 , for example) and electricity. Solid oxide fuel cells have been extensively developed for stationary power generation applications, with early applications such as reliable energy sources for data centers. Solid oxide electrolysis cells are also being developed for converting excess renewable electricity, from intermittent sources such as solar and wind power, 4 to fuels. Reversible operation — storing chemical energy in electrolysis mode and subsequently generating electricity in fuel cell mode — is being explored as a means to help balance grid electricity supply/demand in the presence of increasing levels of intermittent renewable sources.

SOCs typically utilize Ni–YSZ fuel electrodes in both common designs – electrolyte-supported cells (ESCs) and fuel-electrode-supported cells (FESCs). FESCs take advantage of the compatibility between Ni–YSZ and YSZ to allow co-firing at high temperature and thereby produce thin supported electrolytes. This has the advantage of providing low ohmic resistances at

intermediate to low temperatures (\leq 700 °C) because of the thin electrolyte and highly conductive Ni-based fuel electrode.^{8–10} Nonetheless, it is desirable to be able to improve the electrochemical characteristics of Ni–YSZ FESCs while retaining the conventional co-firing approach. This can be achieved by adding a catalyst after high-temperature co-firing. This is typically done by solution infiltration followed by mild heat-treatment, but atomic layer deposition and electrodeposition have also been reported.^{11–13}

Catalytic additions to Ni-YSZ include metals (e.g., Sn, Ni), fluorite-type Ce-based oxides, and perovskite-type oxides. 14-22 CeO₂-based compounds are promising additives because they do not react with Ni or interdiffuse with YSZ at normal SOC operating conditions. Surface modification with doped CeO₂ has been suggested to thermally and chemically stabilize the Ni surface and inhibit the deposition of impurities coming from chemical fuels and/or gas sealants. 14,21,22 Chen et. al. reported enhanced electrochemical performance as well as high sulfur/carbon tolerance for Mo_{0.1}Ce_{0.9}O_{2+δ} impregnated Ni-YSZ.15 More recently, Ovtar et. al. reported that Ce_{0.8}Gd_{0.2}O_{2-δ} (GDC) infiltration reduced the polarization resistance and degradation rate of Ni-YSZ in FESCs during electrolysis.14 However, relatively little is known regarding the mechanisms whereby ceria-based surface modifiers affect electrochemical mechanisms in Ni-YSZ. Furthermore, there is a lack of

Department of Materials Science and Engineering, Northwestern University, Evanston, Illinois 60208, USA. E-mail: s-barnett@northwestern.edu
† Electronic Supplementary Information (ESI) available: See
DOI: 10.1039/x0xx00000x

information about the ceria-modified Ni–YSZ polarization behavior in FESCs over the wide range of fuel compositions encountered during fuel cell and electrolysis operation.

Here we report a detailed investigation of the electrochemical mechanisms of Ni-YSZ electrodes modified by GDC infiltration, studied over a wide range of fuel compositions and temperatures. Ni-YSZ-supported symmetric cells were studied to exclude complicating effects from the oxygen electrode present in full cell tests. The results are also compared with those for electrolyte-supported symmetric cells. The comparison proves useful for defining the effects of gas diffusion through the thick Ni-YSZ support layer in the FESCs. The resultant EIS data are analyzed using a distribution of relaxation times (DRT) approach in order to obtain a physically based model for the impedance responses that includes gas diffusion and a transmission line model incorporating surface reactions and oxygen ion transport. In addition, full FESCs with and without GDC infiltration are compared to confirm the efficacy of GDC for enhancing performance under actual fuel cell and electrolysis operating conditions.

2. Results and discussion

2.1 The effect of GDC concentration

GDC infiltration was done in a single step from aqueous nitrate solutions of GDC precursors with different concentrations, 0.1, 0.5, 1, and 2 mol L⁻¹. These solutions are referred to as GDC0.1, GDC0.5, GDC1, and GDC2, respectively. Fig. 1 shows SEM fracture cross sectional images of Ni-YSZ functional layers after infiltration with different GDC solution molarities, heating to temperature, and electrochemical characterization in 3 vol.% H₂O-humidified H₂ at 600-800 °C for ~2 h. Note that prior studies have already established that this infiltration process yields the desired GDC phase, and that they do not react with Ni or YSZ under the conditions utilized here. 14,21,22 GDC nanoparticles are readily observed on internal pore surfaces for ≥ 0.5 M GDC solutions, but there are only a few small GDC nanoparticles apparent for Ni-YSZ:GDC0.1. The nanoparticle size and coverage generally increased with increasing GDC solution molarity. Comparison of SEM images taken at different locations within the electrodes shows that the GDC particles are uniformly distributed. Images of the Ni-YSZ support layers (Fig. S1 in the Supporting information) generally look similar. Thus, the infiltration process was able to produce GDC nanoparticles throughout the Ni-YSZ support and functional layer. Note that the morphological features of electrodes in electrode-supported cells (Fig. S2) are almost identical to those in Fig. 1, not surprising because they were prepared from the same slurry and fired under the same conditions.

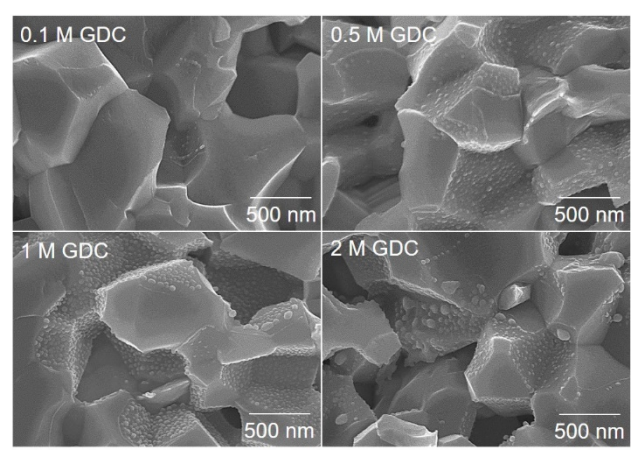


Fig. 1 Cross-sectional SEM images of the surface-modified Ni–YSZ functional layers (after electrochemical characterization): pristine; (single-step) infiltration of 0.1 M GDC; infiltration of 0.5 M GDC; infiltration of 1 M GDC; and infiltration of 2 M GDC.

Fig. 2 shows Nyquist plots of the EIS spectra (after inductance subtraction) for the FESCs and ESCs with different concentrations of GDC solutions infiltrated, including best fits to the data using the equivalent circuit model (ECM) discussed later (Fig. 5). The measurements were carried out in 3 vol.% H₂O-humidified H₂ at 600−800 °C. Fig. 3 summarizes the polarization resistance (R_p) taken from the Nyquist plot high and low frequency intercepts, for the FESCs and ESCs. Across all temperatures, the R_p values were decreased by infiltration of GDC into Ni-YSZ; 0.1 M GDC produced a substantial decrease, with the minimum value at 0.5 M GDC for the FESC, but slight increases for further increases in molarity. Similarly to the FESC, the R_p values in the ESC were found to decrease by addition of GDC with minimum values found at 1 M GDC. In general, the R_p values were much lower for the ESCs than the FESCs. The reduction in R_p becomes more significant with decreasing temperature, i.e., GDC infiltration is especially effective at reduced temperatures.

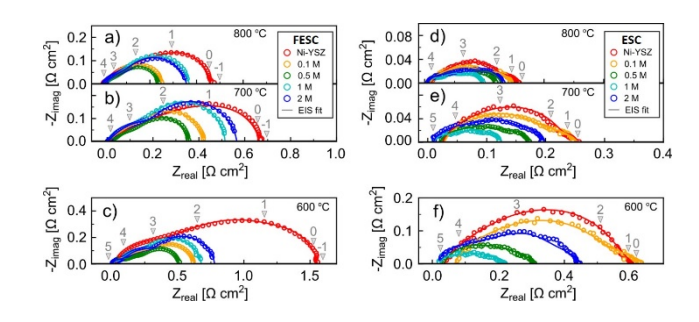


Fig. 2 Nyquist plots of the impedance spectra measured for the FESCs with different concentrations of GDC solutions infiltrated at (a) 800, (b) 700, and (c) 600 °C, and for the ESCs at (d) 800, (e) 700, and (f) 600 °C. All the spectra include the best fits (solid lines) to the data using the equivalent circuit later described in Fig. 5. The number labels $(-1 \le n \le 5)$ above each impedance spectrum give the frequency in 1×10^n Hz. The measurement was carried out in a 3 vol.% H₂O-humidified H₂.

Journal Name ARTICLE

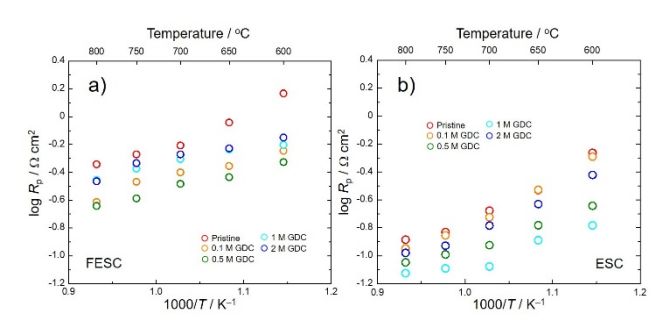


Fig. 3 Temperature-dependences of the polarization resistance (R_p) determined from the impedance data for the (a) FESCs and (b) ESCs with different concentrations of GDC solutions infiltrated.

Since SOC electrode polarization processes (P_x) are often overlapped in EIS spectra, DRT analysis is used to help separate and understand the electrochemical mechanisms. EIS data such as that shown in Fig. 2 were utilized for the DRT calculation. The DRT results for FESCs are compared with those for ESCs in Fig. 4. The present DRT analysis coupled with data reported in previous literature suggests the following four distinct processes observed in all FESC and ESC spectra:²³ (i) P_{GB} ($^{\sim}$ 10⁴ Hz), associated with the grain boundary resistance in the YSZ phase of the Ni–YSZ electrode; (ii) $P_{O^{2-}}$ ($^{\sim}$ 10²–10³ Hz), correlated to oxygen vacancy transport within the YSZ phase of the Ni–YSZ electrode; (iii) P_{rxn} ($^{\sim}$ 10¹–10² Hz), representing the electrode/gas interfacial reaction; and (iv) P_{gas} ($^{\sim}$ 1–3 Hz), representing gas diffusion in the fuel-electrode support layer (FESL) and in the stagnant gas layer (SGL) above the electrode.²³

The GDC infiltration decreases responses in the midfrequency range, namely P_{GB} , $P_{O^{2-}}$, and P_{rxn} , for both types of symmetric cells. The decrease in P_{rxn} is expected based on prior work,14,15,20 and is explained by additional TPB length or reaction area provided by the GDC nanoparticles. GDC also decreases P_{O²⁻}; apparently it enhances the ionic conductivity normally associated with YSZ, perhaps via surface conductivity amongst infiltrated particles. The process at high frequency PGB decreases slightly with increasing GDC content; while the infiltration is not expected to directly impact a grain boundary process, it may indirectly decrease PGB if the GDC conduction short-circuits the ionic conduction through YSZ. The small additional response in the frequency range of Prxn for Ni-YSZ:GDC1.0 is probably associated with diffusion limitations in the porous fuel-electrode, since it becomes visible at a higher frequency than gas diffusion in the support.²³ For the ESCs, P_{gas} is almost negligible and remains constant, regardless of temperature. In contrast, the FESCs show relatively large P_{gas} resistances. The observed temperature dependence of P_{gas} is not normally expected, but could be explained by an overlapping of the gas conversion and gas diffusion processes at low frequency (~ 1 Hz).24

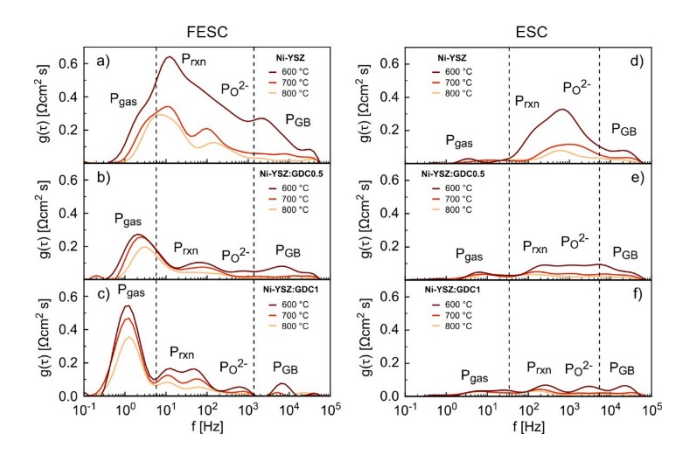


Fig. 4 Distribution of Relaxation Times (DRT) of the EIS spectra obtained from FESCs with (a) pristine Ni–YSZ, (b) Ni–YSZ:GDC0.5, and (c) Ni–YSZ:GDC1. DRT of the EIS spectra obtained from ESCs with (d) pristine Ni–YSZ, (e) Ni–YSZ:GDC0.5, and (f) Ni–YSZ:GDC1.

Based on the above DRT observations, the physically meaningful ECM represented in Fig. 5 was developed, where $R_{\rm ohm}$ is associated with the ionic resistance of the electrolyte and $RQ_{\rm GB}$ (RQ: a resistance R in parallel with a constant phase element Q) is associated with $P_{\rm GB}$. The processes $P_{\rm O^{2-}}/P_{\rm rxn}$, which can be regarded as the main factors limiting the hydrogen oxidation reaction (HOR) and steam reduction reaction (SRR), were included in a simplified transmission line model (TLM) based on a simplified electrode structure consisting of cylindrical pores with length L (the electrode thickness) together with percolated networks of ionically conducting (YSZ) and electronically conducting (Ni) particles. $^{23,25-27}$ Given that the electrode's electronic resistance (R_{e^-}) is much lower than the oxygen ionic resistance ($R_{O^{2-}}$), the impedance of simplified TLM can be described:

$$Z_{\rm TLM} = \lambda R_{\rm O^{2-}} \coth(L/\lambda); \ \lambda = \sqrt{\varsigma/R_{\rm O^{2-}}}$$
 (1)

where ζ represents the RQ element modeling the electrode/gas interface. Lastly, the low frequency (gas diffusion) region is modeled by a generalized finite length Warburg element W having the following impedance:²⁸

$$Z_{\rm W} = R_{\rm W} \frac{\tanh[(j\omega\tau_{\rm W})^{n_{\rm W}}]}{(j\omega\tau_{\rm W})^{n_{\rm W}}} \tag{2}$$

where, $R_{\rm W}$ is the dc diffusion resistance, $n_{\rm w}$ is an exponent (0 < $n_{\rm w}$ < 0.5) implying the degree of non-uniform diffusion, and the diffusion coefficient D of the species is calculated from the time constant $\tau_{\rm w}$ as:

$$\tau_{\rm W} = \frac{L^2}{D} \quad (3)$$

For the FESCs, *L* is the thickness of the fuel-electrode support layer and the effective diffusion coefficient in the porous structure is given by

$$D = D_{H2/H2O} \cdot \frac{\varepsilon}{\tau} \quad (4)$$

where $D_{\rm H_2/H_2O}$ is the diffusivity of the H₂/H₂O mixture, ε is the porosity of the FESL, and τ is its pore tortuosity. ε and τ of the

FESL were determined to be ~0.35 and ~1.52, respectively, by a stereological analysis of electrode images (presented in Fig. S3). For the ESCs, diffusion through the thin Ni–YSZ layer is fast such that mass transport is limited instead by the stagnant gas layer above the electrode, with diffusion coefficient $D = D_{\rm H_2/H_2O}$ and unknown thickness L.

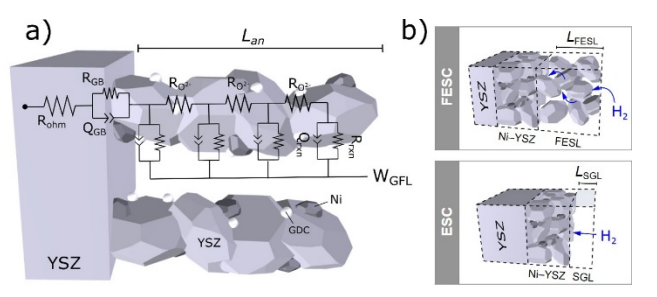


Fig. 5 A diagram illustrating the idealized electrode structure and the associated equivalent circuit model (ECM).

The above model was used to fit the impedance spectra employing a complex nonlinear least squares (CNLS) fitting method. The resultant fits to the EIS spectra are presented in Fig. 2. Fig. 6 illustrates the three components in the fits for the example of cells infiltrated with 0.5 M GDC measured at 600 °C in 3 vol.% H_2O -humidified H_2 . The \emph{RQ}_{GB} element is small but clearly discernable in both the FESC and ESC. The TLM-derived spectrum at intermediate frequencies exhibits a semicircle coupled with a 45° line in the Nyquist plot that implies the combination of hydrogen/steam surface reaction at the electrode/gas interface and the charge (O²⁻) transport. The most noticeable difference between FESC and ESC in Fig. 6 is the much smaller Warburg gas diffusion resistance $R_{\rm W}$ for the ESC. Although this makes sense given that the electrode is much thinner (20 μm vs. 350 μm) for the ESC, a calculation using eqns (2)–(4) with ε = 0.2 and τ = 1.89 for the ESC fuel electrode yields $R_{\rm W}$ much smaller than measured (Fig. 6b).²⁹ Thus, we suggest that the Warburg response in the ESC arises mainly from diffusion through a stagnant gas layer over the fuel electrode.²³ Using the $D_{\mathrm{H_2/H_2O}}$ value obtained from fitting the FESC results, the stagnant gas layer thickness on the ESC is estimated to be ~500 µm. Additionally, a quantitative test to determine the TPB line-specific resistance R_{LS} for the YSZ phase was performed using the data extracted from the TLM and from 3D tomography. R_{LS} showed good agreement with the values found in literature when calculated by EIS analysis (see Fig. S4).30

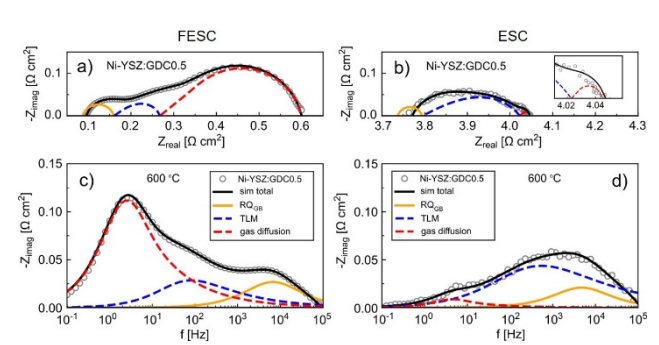


Fig. 6 Nyquist plots of EIS data measured at 600 °C in 3 vol.% H_2O -humidified H_2 from the (a) FESC and (b) ESC with Ni–YSZ:GDC0.5s. Bode plots of EIS data from the (c) FESC and (d) ESC with Ni–YSZ:GDC0.5s. The yellow solid line and the blue/red dashed lines represent RQ_{GB} , TLM, and gas diffusion, respectively, and the black solid line represents the overall fitting.

Fig. 7 summarizes how the key electrode processes are affected by different infiltrated GDC solution concentrations. The $R_{\mathrm{O}^{2-}}$ and R_{rxn} values were noticeably reduced by the GDC infiltration. This might be explained as follows. 14,23,31,32 For Ni-YSZ, the electrochemically active regions are typically restricted to TPBs (Ni|YSZ|gas). The presence of mixed-conducting GDC nanoparticles on the Ni-YSZ surface may enlarge the HOR/SRR active site area, reducing R_{rxn} . The high oxygen ion conductivity of GDC may also provide a parallel pathway for oxygen ion transport in addition to the YSZ, reducing $R_{\mathrm{O}^{2-}}$. The increase in $R_{\rm rxn}$ seen at high GDC solution molarity suggests that the excessive GDC nanoparticles could reduce the GDC surface area or cover key surface sites such as Ni-YSZ TPBs. The gas diffusion resistance gradually increases with increasing the GDC concentration; this is expected because the effective gas diffusivity is proportional to the electrode pore volume fraction, which decreases as the pores become increasingly filled with GDC.

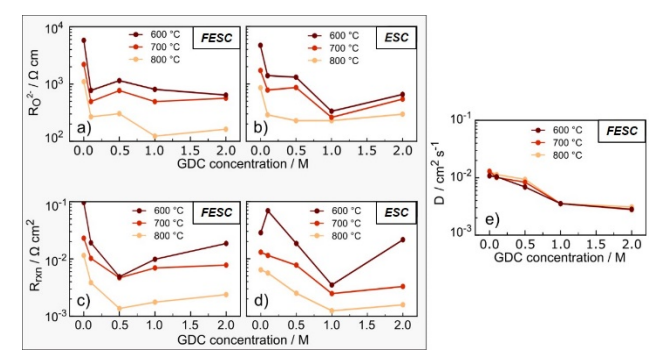


Fig. 7 (a,b) $R_{\rm O^{2-}}$ and (c,d) $R_{\rm rxn}$ values as a function of GDC concentration at different temperatures for the fuel-electrode-supported (a,c) and electrolyte supported cells (b,d). (e) $D_{\rm gas}$ values as a function of GDC concentration at different temperatures for the fuel-electrode-supported cell. $R_{\rm O^{2-}}$ is

Journal Name ARTICLE

normalized to the geometrical electrode area and divided by the electrode thickness L (~20 μ m).

2.2 The effect of steam content on FESCs

The fuel composition in a SOC stack typically varies over a wide range.33,34 Thus, it is important to know the fuel electrode characteristics at different H₂/H₂O ratios. Here we describe EIS measurements on FESCs with Ni-YSZ and Ni-YSZ:GDC0.5 electrodes for a range of H₂O/H₂ ratios from 10%/90% to 90%/10% and temperatures from 600-800 °C. Fig. 8 shows Nyquist plots of selected EIS data measured at 600 °C (see Fig. S5 for the EIS data at 700 and 800 °C), including best fits to the data using the ECM in Fig. 5. Fig. 9 summarizes R_p values of both electrodes at different fuel compositions as a function of temperature. Similarly to the data reported in previous literature concerning the steam effect on Ni-YSZ electrode performance, 23,31,32 all R_p values decreased with increasing the steam content at each temperature. The Ni-YSZ:GDC0.5 yields lower R_p in all cases, but especially at lower temperature. Although the overall trend is for R_p to decrease with increasing steam content, the high-frequency response for 600 and 700 °C actually increases for Ni-YSZ:GDC0.5 when the steam content is increased above 10 vol.%; this is offset by a substantial decrease in the low frequency response.

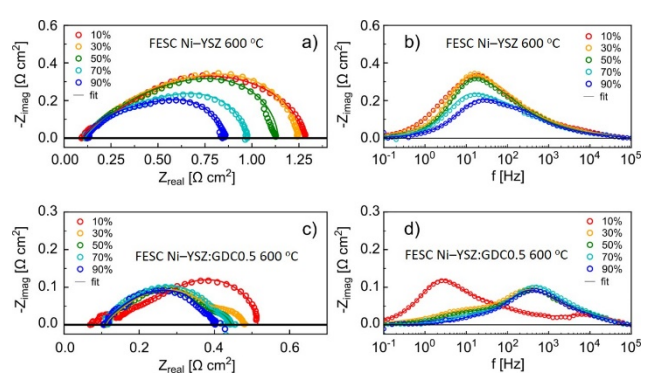


Fig. 8 Nyquist and Bode plots comparing selected impedance spectra for FESCs with (a,b) Ni–YSZ and (c,d) Ni–YSZ:GDC0.5, measured at 600 $^{\circ}$ C with steam content in H₂ varied from 10 to 90 %. All the spectra include the best fits (solid lines) to the data using the equivalent circuit described in Fig. 5.

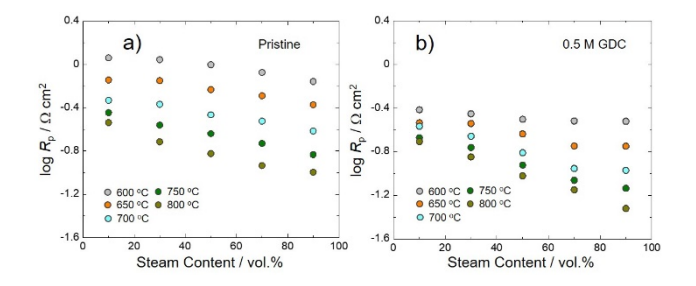


Fig. 9 Polarization resistance (R_p) vs. steam content at different temperatures for the FESCs with (a) pristine and (b) 0.5 M GDC-infiltrated Ni–YSZs.

The effect of the H₂O-H₂ mixture on the electrochemical mechanisms were analyzed using the ECM described in Fig. 5. The fits are shown in Fig. 8 for the FESC with Ni-YSZ and Ni-YSZ:GDC0.5 at 600 °C, and for the other temperatures in Fig. S5. The electrical parameters from the fitting are compared at 600 °C in Fig. 10 and for the other temperatures in Fig. S6. The infiltrated cell exhibits much lower values of $R_{\Omega^{2-}}$ and R_{rxn} at low steam content (consistent with the data taken at 3 vol.% H₂O in Fig. 7) and low temperature, but the difference narrows at higher steam contents and temperatures. Starting with Ni-YSZ, $R_{\Omega^{2-}}$ and R_{rxn} both decrease with increasing steam content. This can be explained by the H₂O-Ni interaction accelerating atomic hydrogen diffusion as well as hydrogen dissociative adsorption on the Ni surface. 23,31,32 Furthermore, the dissociative adsorption of H2O on YSZ near TPBs can help decrease $R_{\rm rxn}$. For Ni–YSZ:GDC0.5, $R_{\rm O^{2-}}$ remains constant regardless of the steam content; however, R_{rxn} increases with increasing steam content and the values are similar for the infiltrated and non-infiltrated electrodes at 90 vol.% H₂O. Noting that the catalytic effect of GDC arises from its mixed conductivity in a reducing atmosphere, the increase in R_{rxn} may reflect that GDC becomes less electronically conductive under high steam, and thereby its catalytic activity decreases. The gas diffusivity increases rapidly with increasing steam content for Ni-YSZ, as expected because higher steam contents are required for effective mass transport given the lower inherent diffusivity of H₂O compared to H₂. A similar trend is observed for Ni-YSZ:GDC0.5, but diffusivity values are lower. This presumably reflects the fact that GDC infiltration reduces the pore volume available for gas diffusion.

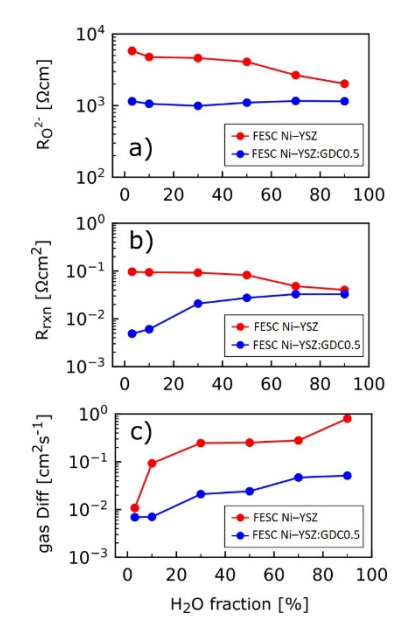


Fig. 10 (a) $R_{\rm O^{2-}}$, (b) $R_{\rm rxn}$, and (c) $D_{\rm gas}$ values as a function of H₂O fraction for the FESCs with Ni–YSZ and Ni–YSZ:GDC0.5 electrodes measured at 600 °C.

2.3 Full cell results

 $Sr(Ti_{0.3}Fe_{0.63}Co_{0.07})O_3$ (STFC) was selected as the oxygen electrode because of its improved electrochemical performance and stability compared with the commonly $(La_{0.6}Sr_{0.4})(Co_{0.2}Fe_{0.8})O_3$ (LSCF) electrode.³⁵ Full FESCs with STFC oxygen electrodes were constructed to evaluate the effect of GDC infiltration under practical operating conditions. Some of these cells had fuel electrode supports similar to those in the above-described symmetrical cells, with ε = ~0.35 (see Fig. S7). Given the significant resistance introduced by gas diffusion in those cells, modified cells with increased support-layer porosity $(\varepsilon = ^{\circ}0.55$; see Fig. S3(b)) were also prepared and tested. Figs. 11(a) and (b) present the current-voltage results for the Ni-YSZ:GDC0.5 electrode cell with ε = ~0.55 – the fuel cell characteristics were measured in 3 vol.% H₂O-humidified H₂ and air (Fig. 11(a)) and the steam electrolysis characteristics in 50 vol.% H₂O-humidified H₂ and air (Fig. 11(b)). For comparison, Fig. S7 shows the corresponding results for the cells with pristine Ni–YSZ and Ni–YSZ:GDC0.5 (ε = ~0.35). The open-circuit voltage (OCV) ranged from ~1.06 at 800 °C to ~1.10 V at 600 °C in 3 vol.% H_2O , and ~0.95 V to ~1.03 V in 50 vol.% H_2O . The GDC-infiltrated cell with ε = ~0.55 yielded fuel cell maximum power density from 0.61 at 600 °C to 2.25 W cm⁻² at 800 °C. The current density at 1.3 V in electrolysis mode ranged from 0.38 at 600 °C to 2.22 A cm⁻² at 800 °C. These values are higher than for the corresponding cells with ε = ~0.35 (Fig. S7); Fig. 11(c) summarizes the performance enhancements due to GDC infiltration, showing a larger percentage power density increase at lower temperature. The comparison of relevant impedance spectra for both cells, presented in Figs. S8 and S9, clearly indicates the R_p reductions arising due to both GDC infiltration and increased support porosity.

Fig. 11(b) shows the expected decrease in cell resistance with increasing temperature in both fuel cell and electrolysis modes. The j-V curves show no obvious indication of limiting current behavior, in contrast with the low-support-porosity cells (ε = ~0.35) shown in Figs. S7(b) and (d), which shows pronounced concentration polarization especially in electrolysis mode. Fig. 11(d) compares the electrolysis current density measured at 1.3 V vs. temperature for the Ni–YSZ and Ni–YSZ:GDC0.5 electrode cells with different support porosity. For low porosity, GDC provides a substantial enhancement at low temperature, but lesser enhancement at higher temperature where the performance is mainly limited by gas diffusion. With the additional support porosity eliminating the gas diffusion limitation, the GDC infiltration provides a continuous increase in current density with increasing temperature. Clearly, the cell performance was improved substantially by increasing the Ni-YSZ support porosity, especially given that GDC infiltration reduces the available pore volume. In summary, these results verify the efficacy of GDC for enhancing the electrochemical performance of Ni-YSZ in full cells. Ni-YSZ fuel electrode degradation was not a focus of this study, but initial full-cell life test results (Fig. S10) show that GDC infiltration improves stability during electrolysis, consistent with prior reports. 14,22

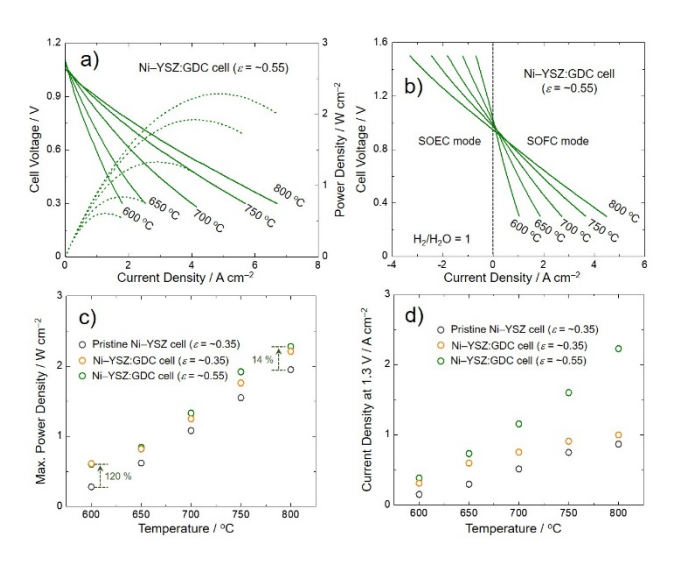


Fig. 11 Electrochemical characteristics of the Ni–YSZ-supported SOC with Ni–YSZ:GDC0.5 ($e = ^{\circ}0.55$) under the (a) typical fuel cell operating condition (3 vol.% H₂O-humidified H₂ and air) and (b) steam electrolysis condition (50 vol.% H₂O-humidified H₂ and air). Comparison of the maximum power densities in (c) fuel cell mode and (d) current densities at 1.3 V in electrolysis mode for the fuel electrode-supported SOCs with Ni–YSZ ($\varepsilon = ^{\circ}0.35$) and Ni–YSZ:GDC0.5 ($\varepsilon = ^{\circ}0.35$) and $^{\circ}0.55$).

3. Conclusions

The present results provide insights into how GDC infiltration affects the electrochemical characteristics of Ni-YSZ fuel electrodes. GDC introduced at an appropriate infiltrate solution concentration substantially reduces the polarization resistance of Ni-YSZ electrodes in both electrolyte-supported and fuel-electrode-supported cells. Analysis of electrochemical impedance spectroscopy data allowed development of a model of the porous electrode, yielding insights into the electrochemical processes:

- GDC infiltration reduces the reaction resistance associated with three-phase boundaries. This is in accord with prior studies,¹⁴ and has generally been explained by an expansion of the TPB density of the electrode;
- In addition, GDC infiltration appears to improve oxygen transport in the electrode. The latter suggest that oxygen ion transport, occurring in or on the surface of the infiltrated GDC phase, can augment than in the YSZ phase;
- 3) The GDC effect is less pronounced in the fuel-electrodesupported cell geometry because the thicker Ni–YSZ layers yielded significant concentration polarization. Indeed, achieving high current density electrolysis operation requires fuel-electrode supports with relatively high porosity;
- Too-large infiltrated GDC amounts exacerbate concentration losses by reducing electrode porosity;

Journal Name ARTICLE

- 5) The effect of GDC was less pronounced at high steam concentrations, probably because GDC tends to lose its electronic conductivity, and hence its catalytic activity, under high steam conditions;
- The gas diffusion resistance decreases with increasing steam content, by allowing relatively faster transport of the relatively slow diffusing H₂O;
- 7) Increasing the H₂O fraction in the H₂–H₂O fuel mixture reduced both the three-phase boundary resistance and the gas diffusion resistance for Ni–YSZ; however, with GDC infiltration, the electrode resistance showed less variation with fuel composition.

4. Experimental

4.1 Cell fabrication

Two different symmetric cell types were prepared: (i) electrolyte-supported (ESCs) and (ii) Ni-YSZ fuel-electrodesupported symmetric cells (FESCs). Both cell types were produced by tape casting and lamination. The electrode functional layer was cast from a slurry containing 50 wt.% NiO-50 wt.% YSZ. The YSZ electrolyte layer was cast from a slurry with YSZ (Tosoh) mixed with 1 mol.% Fe₂O₃ sintering aid. For the ESCs, the final fired thicknesses were ~400 µm for the YSZ electrolyte and ~20 µm for the Ni-YSZ functional layers. The support layer for the FESCs was cast from a slurry containing 45 wt.% NiO-45 wt.% YSZ-10 wt.% starch. In some cases, the porosity of the support layer was increased by adding additional graphite pore former, with the composition 39 wt.% NiO-39 wt.% YSZ-10 wt.% starch-12 wt.% graphite. For the FESCs, the final fired thicknesses for the YSZ electrolyte, Ni-YSZ functional layers, and Ni–YSZ support layers were ~8, ~20, and ~350 μm , respectively. The tape lamination was carried out at 70 °C for 5 minutes under a pressure of ~22 atm. The resultant laminates were co-sintered at 1250 °C for 4 h.

For the fabrication of fuel electrode-supported full cell, NiO–YSZ supported half-cells were first prepared through tape casting, lamination, and pre-sintering (at 1150 °C for 2 h). The 3 mol.% Fe₂O₃-doped GDC layers were formed on the YSZ surfaces of half-cells *via* dip-coating process, followed by cosintering at 1250 °C for 4 h. Note that the desirable amounts of Fe₂O₃ (Alfa Aesar, 99.8 %) were added into the YSZ and GDC to obtain a sufficiently high density at the 1250 °C firing temperature. ²⁹ The final fired thicknesses of support, functional layer, YSZ electrolyte, and GDC layer were approximately 350, 20, 8, and 1 μ m, respectively. The 8- μ m thick STFC layers (active area: 0.5 cm²) were screen-printed onto the GDC electrolyte layers of the half-cells and then sintered at 1050 °C at 3 h (See Fig. S11).

4.2 GDC infiltration

The GDC solutions were prepared by dissolving desired amounts of $Gd(NO_3)_3 \cdot 6H_2O$ and $Ce(NO_3)_3 \cdot 6H_2O$ in distilled water. Triton X-100 and citric acid were additionally added into the GDC precursor solution as a surfactant and a chelating agent, respectively. The cells were pre-reduced with 3 vol.% H_2O -

humidified H_2 at 700 °C for 5 h to obtain sufficiently porous Ni–YSZ structure for the penetration of GDC precursor solution. Symmetric cells were pre-reduced in a furnace, whereas the full cells were reduced in the cell test setup in which the cell could be removed for infiltration followed by re-sealing into the testing rig. The cell microstructure after reduction is similar to that reported previously, and is shown in Fig. S12. Infiltration of 10 μ l of GDC solution into the porous scaffold was then carried out followed by *in situ* thermal conversion during the SOFC startup, *i.e.*, by heating in 3 vol.% H_2 O-humidified H_2 at 5 °C/min to 600 °C. It appears that the nitrate and organic components of the infiltrate were effectively removed by this procedure prior to cell testing, which is similar to that employed previously. 14,21,22

4.3 Electrochemical characterization

For the symmetric cell testing, Ni-meshes adhered to both Ni-YSZ support by using Ag paste (DAD-87, Shanghai Research Institute of Synthetic Resins) for current collection. The electrochemical impedance spectroscopy (EIS) was carried out at 600–800 °C in various $\rm H_2O-H_2$ mixtures with steam content from 3 vol. % to 90 vol.%. The EIS data were collected under open circuit conditions with an IM6 Electrochemical Workstation (ZAHNER) by using a 20 mV ac signal in the frequency range of from 0.1 Hz to 100 kHz. The complex nonlinear least squares fitting of the EIS data and simulations of the individual circuit elements were performed using software programmed in Python that relies on the scientific Python stack. $^{36-38}$

For the full cell testing, the gold grids (Heraeus) were screen-printed on the STFC oxygen electrodes for current collection. The cells were mounted/sealed on alumina tubes using silver paste. During the electrolysis testing (or fuel cell testing), 50 vol.% H_2O (or 3 vol.% H_2O) humidified hydrogen and air were supplied into the fuel and oxygen electrodes, respectively. The polarization (current vs. voltage) curves and the impedance spectra of the cells were obtained at $600-800\,^{\circ}C$.

4.4 Materials characterization

The microstructural observation was performed on the posttest cells through scanning electron microscopy (SEM, Hitachi S-4800).

Conflicts of interest

There are no conflicts to declare.

Acknowledgements

The authors gratefully acknowledge research support from the HydroGEN Advanced Water Splitting Materials Consortium, established as part of the Energy Materials Network under the U.S. Department of Energy, Office of Energy Efficiency and Renewable Energy, Fuel Cell Technologies Office, under Award Number DE-0008079. The electrochemical modeling work was supported financially by the Department of Energy National

Energy Technology Laboratory under Prime Award Number DE-FE0027584 to FuelCell Energy, Inc., and under Subaward to Northwestern University. Some of the microstructural characterization was supported by National Science Foundation grants DMR-1506925 and DMR-1912530.

References

- 1 D. M. Bierschenk, J. R. Wilson and S. A. Barnett, *Energy Environ. Sci.*, 2011, **4**, 944-951.
- 2 E. Masanet, A. Shehabi and J. Koomey, Nat. Clim. Change, 2013, 3, 627.
- K. Caldeira, A. K. Jain and M. I. Hoffert, Science, 2003, 299, 2052-2054.
- 4 M. Z. Jacobson, M. A. Delucchi, Z. A. F. Bauer, S. C. Goodman, W. E. Chapman, M. A. Cameron, C. Bozonnat, L. Chobadi, H. A. Clonts, P. Enevoldsen, J. R. Erwin, S. N. Fobi, O. K. Goldstrom, E. M. Hennessy, J. Liu, J. Lo, C. B. Meyer, S. B. Morris, K. R. Moy, P. L. O'Neill, I. Petkov, S. Redfern, R. Schucker, M. A. Sontag, J. Wang, E. Weiner and A. S. Yachanin, *Joule*, 2017, 1, 108-121.
- C. Graves, S. D. Ebbesen, S. H. Jensen, S. B. Simonsen and M. B. Mogensen, *Nat. Mater.*, 2014, 14, 239.
- 6 N. Xu, X. Li, X. Zhao, J. B. Goodenough and K. Huang, Energy Environ. Sci., 2011, 4, 4942-4946.
- 7 B.-K. Park, Q. Zhang, P. W. Voorhees and S. A. Barnett, *Energy Environ. Sci.*, 2019, **12**, 3053-3062.
- 8 N. Q. Minh and T. Takahashi, in *Science and Technology of Ceramic Fuel Cells*, eds. N. Q. Minh and T. Takahashi, Elsevier Science Ltd, Oxford, 1995, DOI: 10.1016/B978-044489568-4/50010-4, pp. 233-306.
- 9 M. C. Tucker, J. Power Sources, 2010, 195, 4570-4582.
- 10 K. Kendall, N. Q. Minh and S. C. Singhal, in *High Temperature and Solid Oxide Fuel Cells*, eds. S. C. Singhal and K. Kendall, Elsevier Science, Amsterdam, 2003, DOI: 10.1016/B978-185617387-2/50025-8, pp. 197-228.
- 11 Y. Gong, R. L. Patel, X. Liang, D. Palacio, X. Song, J. B. Goodenough and K. Huang, *Chem. Mater.*, 2013, **25**, 4224-4231.
- 12 B.-K. Park, S.-B. Lee, T.-H. Lim, R.-H. Song and J.-W. Lee, *ChemSusChem*, 2018, **11**, 2620-2627.
- 13 D. Ding, X. Li, S. Y. Lai, K. Gerdes and M. Liu, *Energy Environ. Sci.*, 2014, **7**, 552-575.
- 14 S. Ovtar, X. Tong, J. J. Bentzen, K. T. S. Thydén, S. B. Simonsen and M. Chen, *Nanoscale*, 2019, **11**, 4394-4406.
- 15 Y. Chen, J. Bunch, C. Jin, C. Yang and F. Chen, *J. Power Sources*, 2012, **204**, 40-45.
- 16 Y. Lu, P. Gasper, U. B. Pal, S. Gopalan and S. N. Basu, J. Power Sources, 2018, 396, 257-264.
- 17 S. Sengodan, M. Liu, T.-H. Lim, J. Shin, M. Liu and G. Kim, *J. Electrochem. Soc.*, 2014, **161**, F668-F673.
- 18 Z. Liu, B. Liu, D. Ding, M. Liu, F. Chen and C. Xia, *J. Power Sources*, 2013, **237**, 243-259.
- M. D. McIntyre, J. D. Kirtley, A. Singh, S. Islam, J. M. Hill and R. A. Walker, *J. Phys. Chem. C*, 2015, **119**, 7637-7647.
- 20 R. Fernández-González, J. C. Ruiz-Morales, J. Canales-Vázquez, J. R. Jurado, A. Makradi and P. Núñez, *Int. J. Hydrogen Energy*, 2016, 41, 19731-19736.
- 21 H. Kurokawa, T. Z. Sholklapper, C. P. Jacobson, L. C. De Jonghe and S. J. Visco, *Electrochem. Solid-State Lett.*, 2007, **10**, B135-B138.
- 22 T. L. Skafte, J. Hjelm, P. Blennow and C. Graves, J. Power Sources, 2018, 378, 685-690.
- 23 T. Ramos, M. Søgaard and M. B. Mogensen, J. Electrochem. Soc., 2014, 161, F434-F444.

- 24 S. Primdahl and M. Mogensen, J. Electrochem. Soc., 1999, 146, 2827-2833.
- 25 J. Nielsen, T. Klemensø and P. Blennow, J. Power Sources, 2012, 219, 305-316.
- 26 V. Sonn, A. Leonide and E. Ivers-Tiffee, ECS Transactions, 2007, 7, 1363-1372.
- 27 R. de Levie, *Electrochim. Acta*, 1964, **9**, 1231-1245.
- 28 A. Leonide, V. Sonn, A. Weber and E. Ivers-Tiffée, *J. Electrochem. Soc.*, 2008, **155**, B36-B41.
- 29 Z. Gao, V. Y. Zenou, D. Kennouche, L. Marks and S. A. Barnett, J. Mater. Chem. A, 2015, 3, 9955-9964.
- 30 W. G. Bessler, M. Vogler, H. Störmer, D. Gerthsen, A. Utz, A. Weber and E. Ivers-Tiffée, Phys. Chem. Chem. Phys., 2010, 12, 13888-13903.
- 31 H. P. Dasari, S.-Y. Park, J. Kim, J.-H. Lee, B.-K. Kim, H.-J. Je, H.-W. Lee and K. J. Yoon, *J. Power Sources*, 2013, **240**, 721-728.
- 32 W. Pan, K. Chen, N. Ai, Z. Lü and S. P. Jiang, *J. Electrochem. Soc.*, 2016, **163**, F106-F114.
- 33 X. Zhang, J. E. O'Brien, R. C. O'Brien, J. J. Hartvigsen, G. Tao and G. K. Housley, *Int. J. Hydrogen Energy*, 2013, **38**, 20-28.
- 34 V. N. Nguyen, Q. Fang, U. Packbier and L. Blum, *Int. J. Hydrogen Energy*, 2013, **38**, 4281-4290.
- 35 S.-L. Zhang, H. Wang, M. Y. Lu, A.-P. Zhang, L. V. Mogni, Q. Liu, C.-X. Li, C.-J. Li and S. A. Barnett, *Energy Environ. Sci.*, 2018, **11**, 1870-1879.
- 36 C. Graves, RAVDAV Data Analysis Software ver.0.9.7, 2012.
- 37 S. v. d. Walt, S. C. Colbert and G. Varoquaux, *Comput. Sci. Eng.*, 2011, **13**, 22-30.
- 38 J. D. Hunter, Comput. Sci. Eng., 2007, 9, 90-95.